Random vibration testing of microelectromechanical deformable mirrors for space-based high-contrast imaging

**Axel Potier [iD],[a,*] Camilo Mejia Prada,[a] Garreth Ruane [iD],[a] Hong Tang,[a]
Wesley Baxter,[a] Duncan Liu,[a] A. J. Eldorado Riggs,[a] Phillip K. Poon,[a]
Eduardo Bendek [iD],[a] Nick Siegler,[a] Mary Soria [iD],[a] Mark Hetzel,[a] Charlie Lam,[b]
and Paul Bierden[b]**

[a]Jet Propulsion Laboratory, California Institute of Technology, Pasadena, California, United States
[b]Boston Micromachines Corp., Cambridge, Massachusetts, United States

ABSTRACT. Space-based stellar coronagraph instruments aim to directly image exoplanets that are a fraction of an arcsecond separated from and 10 billion times fainter than their host star. To achieve this, one or more deformable mirrors (DMs) are used in concert with coronagraph masks to control the wavefront and minimize diffracted starlight in a region of the image known as the "dark zone" or "dark hole (DH)." The DMs must have a high number of actuators (50 to 96 across) to allow for DHs that are large enough to image a range of desired exoplanet separations. In addition, the surfaces of the DMs must be controlled at the picometer level to enable the required contrast. Any defect in the mechanical structure of the DMs or electronic system could significantly impact the scientific potential of the mission. Thus NASA's Exoplanet Exploration Program procured two 50×50 microelectromechanical DMs manufactured by Boston Micromachines Corporation to test their robustness to the vibrational environment that the DMs will be exposed to during launch. The DMs were subjected to a battery of functional and high-contrast imaging tests before and after exposure to flight-like random vibrations. The DMs did not show any significant functional nor performance degradation at 10^{-8} contrast levels.

1 Introduction

The 2020 Decadal Survey on Astronomy and Astrophysics[1] prioritized the development of technologies for directly imaging Earth-like exoplanets with the future Habitable World Observatory (HWO) flagship mission. The document recommended a large (∼6 m) infrared/optical/ultraviolet telescope with a stellar coronagraph or starshade to be launched in the first half of the 2040s. If a coronagraph instrument is selected, it will be designed to attenuate the diffracted light from the host star to create a region of high contrast in the image [known as the "dark zone" or "dark hole (DH)"] where exoplanets that are ∼10^{10} times fainter than the star may be imaged at angular separations of <1 arc sec. To accomplish this, a series of coronagraph masks and one or more deformable mirrors (DMs) will be used to minimize the stellar intensity in the DH.[2,3]

---

*Address all correspondence to Axel Potier, axel.q.potier@jpl.nasa.gov

DM technologies are being developed for both ground- and space-based high-contrast imaging applications. Electrostrictive devices[4,5] and microelectromechanical (MEMS)[6–8] systems are the most advanced for space applications and have been at least partially flight qualified. On the one hand, the Roman Space Telescope (RST) Coronagraph Instrument will make use of two 48 × 48 electrostrictive devices manufactured by Adaptive Optics Associates (AOA) - Xinetics.[9] These DMs have proven to have a high reliability and high performance, but the contact between the electrodes and the reflective face sheet may increase the potential for unwanted motions due to thermal variations. Moreover, these devices have a relatively large (≥1 mm) interactuator pitch. On the other hand, MEMS DMs have also demonstrated a promising performance.[10–12] Their contactless technology mitigates hysteresis and other instabilities caused by environmental factors and allows for a smaller pitch (0.3 to 0.4 mm), which makes them attractive candidates for the future HWO mission.[13,14] However, the technological readiness of the MEMS DMs lags behind the electrostrictive DMs that will be demonstrated in flight by RST. Indeed, lead magnesium niobate electroceramic actuators (PMN), manufactured by AOA Xinetics, have successfully completed the full space qualification process for use in the RST Coronagraph Instrument. However, the mechanical construction differs, making it impossible to transfer the heritage to MEMS devices.

Boston Micromachines Corporation (BMC) MEMS DMs have been extensively tested in vacuum at high-contrast imaging testbed (HCIT) demonstrating their ability to function and endure in a vacuum. However, it was found that the absence of air allows the residual high-frequency electrical noise to cause mechanical resonance of the DM membrane. This issue was resolved by implementing RC filters on each channel to dampen the electrical noise before it induced mechanical vibration.[8] Thereafter, proper operation in a vacuum chamber was successfully demonstrated.[12]

The next milestone in space qualification for the MEMS DM is proving its ability to survive the General Environmental Verification Standard vibration profile. Assessing the survivability and operational capabilities of DMs during launch and in space would require multiple additional stages. Therefore, before allocating more resources for further tests, such as acoustics, shock, radiation, and EMI, we first sought to confirm the MEMS DM's endurance under these conditions. Prior attempts to evaluate MEMS vibration survivability revealed that the tested devices exhibited altered behavior following the shake and vibe process.[15] However, after discussing the experimental setup with the authors, we concluded that the change might have been caused by other factors, such as particle contamination. Lacking sufficient information to evaluate the MEMS DM's vibration resistance, we decided to conduct a new study, which is presented in this paper.

In that context, and as part of a NASA Small Business Innovation Research (SBIR) project titled "Improved Yield, Performance, and Reliability of High-Actuator-Count Deformable Mirrors," BMC developed a new fabrication process and several design modifications that were integrated in a complete fabrication cycle, producing fully operational 2040-actuator continuous face-sheet MEMS DMs.

With support from NASA's Exoplanet Exploration Program's coronagraph technology development efforts, several sets of these DMs were tested for reliability in a flight-like environment. Expanding on our previous results,[16] this paper reports on experiments carried out at the HCIT facility at NASA's Jet Propulsion Laboratory to demonstrate the robustness of BMC's MEMS DM technology to random vibrations during rocket launch. In Sec. 2, we present the manufacturing and integration of these DMs and their design from the dedicated electronics to the DM face-sheet. In Sec. 3, we describe the workflow of the tests performed in HCIT and the different facilities used in these experiments. Finally, Sec. 4 presents the results that demonstrate the survivability and robustness of high-actuator-count MEMS DMs to random vibrations.

2 Design and Fabrication of the MEMS DMs

2.1 DM Design and Wafer Fabrication

For this study, we procured two 2040-actuator DMs from BMC with the characteristics specified in Table 1; the layout is illustrated in Fig. 1. The DMs were manufactured on 1.1 mm thick

Table 1 High-actuator-count MEMS DM properties.

# of actuators in active area	2040
# of actuators across the active area	50
Pupil diameter	19.6 mm
Actuator pitch	400 μm
Substrate thickness	1.1 mm
Actuator stroke	1.0 μm
Operating voltage	0 to 98 V
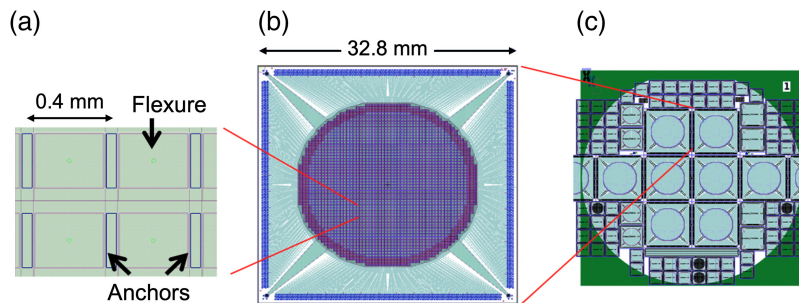
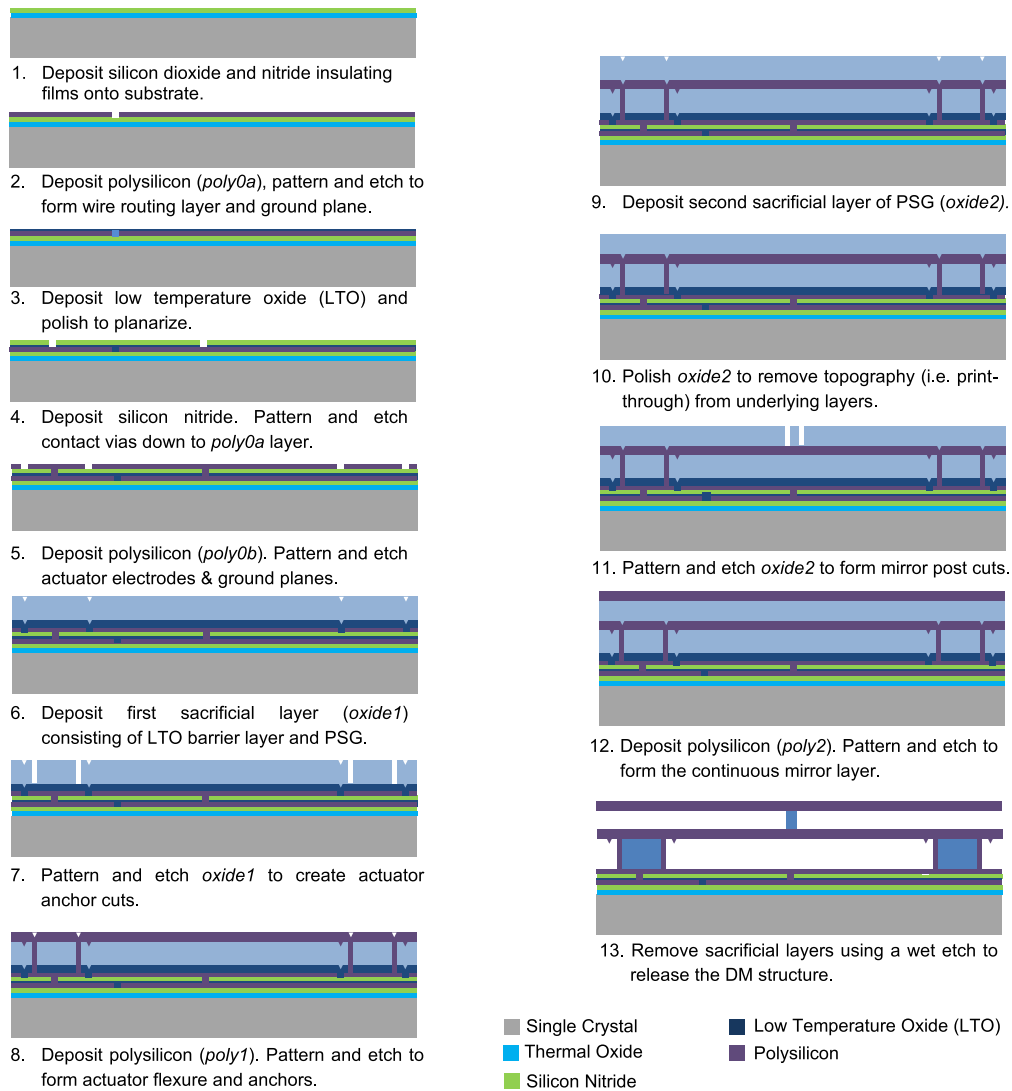**Fig. 1** Diagram of the devices under test. (a) A zoomed-in view of a 2 × 2 actuator region. Each actuator (0.4 mm across) consists of a flexure anchored at its edges. (b) The full DM layout with 2040 actuators as well as wire traces extending radially to the edges of the 32.8 mm substrate. (c) The full wafer layout as manufactured, which typically has several DMs of different formats to make best use of the available wafer area.

substrates that are more than four times stiffer than the standard substrate. This thickness was optimized through a finite-element analysis studying the stresses on the mirror caused by random vibrations using conservative RST coronagraph instrument flight acceptance specifications (see blue curve in Fig. 7). It brings about a higher resistance to bending stresses exerted by the thin films. This change also reduces the surface deformation of the unpowered DM and then increases the DM usable stroke for wavefront control (WFC) after flattening. BMC developed custom tooling at the commercial MEMS foundry to work with the new substrate and process these thicker wafers.

Other than the substrate thickness, no step in the manufacturing process is different from usual BMC DMs. The procedure, illustrated in Fig. 2, is as follows.

(i) Silicon dioxide and a low-stress silicon nitride layer were deposited on a single-crystal silicon substrate to electrically insulate the conductive substrate from the MEMS devices (Fig. 2, step 1).

(ii) The first layer of polysilicon (referred to as Poly 0a) was then deposited, patterned, and etched to create actuator base electrodes and wire routing for the array (Fig. 2, step 2).

(iii) A low-temperature oxide (LTO) layer was deposited and polished using chemomechanical polishing techniques to flatten the layer. A second dielectric film, low-stress silicon nitride was then deposited (Fig. 2, step 3–4).

(iv) The LTO and silicon nitride layer was lithographically patterned and etched to provide a path for electrical connectivity between the wire traces, actuator electrodes, and grounded landing pads, which were produced in a subsequent polysilicon thin film (Poly 0b) deposition and patterning process (Fig. 2, step 4).

(v) An array of actuator electrodes was fabricated (Fig. 2, step 5). Then a thick sacrificial layer (oxide 1) made up of phosphosilicate glass and a thin barrier layer of LTO were deposited

1. Deposit silicon dioxide and nitride insulating films onto substrate.

2. Deposit polysilicon (*poly0a*), pattern and etch to form wire routing layer and ground plane.

3. Deposit low temperature oxide (LTO) and polish to planarize.

4. Deposit silicon nitride. Pattern and etch contact vias down to *poly0a* layer.

5. Deposit polysilicon (*poly0b*). Pattern and etch actuator electrodes & ground planes.

6. Deposit first sacrificial layer (*oxide1*) consisting of LTO barrier layer and PSG.

7. Pattern and etch *oxide1* to create actuator anchor cuts.

8. Deposit polysilicon (*poly1*). Pattern and etch to form actuator flexure and anchors.

9. Deposit second sacrificial layer of PSG (*oxide2).*

10. Polish *oxide2* to remove topography (i.e. print-through) from underlying layers.

11. Pattern and etch *oxide2* to form mirror post cuts.

12. Deposit polysilicon (*poly2*). Pattern and etch to form the continuous mirror layer.

13. Remove sacrificial layers using a wet etch to release the DM structure.

Single Crystal   Low Temperature Oxide (LTO)
Thermal Oxide   Polysilicon
Silicon Nitride

Fig. 2 BMC's MEMS DM fabrication process.

on the Poly 0b layer to create the actuator gap (Fig. 2, step 6). The stroke of the electrostatic actuators depends on its thickness.

(vi) The oxide 1 film was patterned and etched once more to create the actuator anchor features (Fig. 2, step 7).

(vii) A second layer of polysilicon, Poly 1, was deposited, patterned, and etched to create actuator anchors and compliant actuator flexures with integrated hard stops (Fig. 2, step 8).

(viii) A second sacrificial layer, oxide 2, was deposited and polished to remove print-through from the underlying films. The mirror attachment post-features were then patterned and etched into the oxide 2 film (Fig. 2, steps 9–11).

(ix) A final polysilicon layer, Poly 2, was then deposited, polished, and patterned (Fig. 2, step 12).

(x) Metal bond-pads were added to allow for wire-bonding of the device and to allow the wafers to be diced into individual DM devices.

(xi) Finally, the sacrificial oxide layers were removed using a wet etch "release" process (Fig. 2, step 13).

Once the devices were received from the foundry, BMC inspected the DMs using visible and IR optical microscopy and interferometry to identify potential optical, electrical, and subsurface

Table 2 Initial surface quality properties of DUT 1 and DUT 2. Unpowered and powered surface errors are domniated by a strong astigmatism, characteristic of MEMS DMs.

|	DUT 1	DUT 2
Initial yield (%)	100	99.3
Unpowered surface deformation (PV/RMS, nm)	604/116	797/100
Maximum powered surface deformation (PV/RMS, nm)	586/113	1382/115
Flat map deformation (PV/RMS, nm)	89/3.4	787/17

manufacturing defects. Using a custom probe station, each candidate die that passed this initial inspection was tested to determine actuator response. Their electromechanical and optical performance were then characterized, including the responsiveness of each actuator, stroke limits, unpowered surface error, and actuator defects.

We selected two devices for this study, which we refer to as device under test (DUT) 1 and 2. Their initial surface properties are summarized in Table 2. DUT 1 is a 100% functional unit that was coated with an evaporated thin film of aluminum at BMC's facility. The purpose of DUT 1 is to confirm or reject the hypothesis that a fully functional 2K MEMS DM can survive a launch environment. On the other hand, DUT 2 has some unresponsive actuators. We kept its face sheet uncoated to allow for the post-vibration infrared inspection of the DM surface to help understand any failure mode. This DUT aimed to test the hypothesis that defects causing anomalous actuators can propagate to neighboring actuators during random vibrations.[16]

2.2 Electrical Connections

For both DUTs, coated-dies were attached with adhesive to a ceramic package specifically designed for the 2K DMs (see Fig. 3). The DM die and the ceramic package were electrically connected using gold wire-bonds applied with a high-precision automated tool at BMC's facility. JPL also fabricated flex cables that were connected in the back of the new chip carrier through a pin-grid array (PGA) and terminated in 528-pin MEG-Array connectors (see Fig. 4).

The packaged DMs were tested using high-voltage drivers commercially available from BMC to characterize their electromechanical and optical performance. BMC's electronics connect to the DM via the MEG-Array connectors.
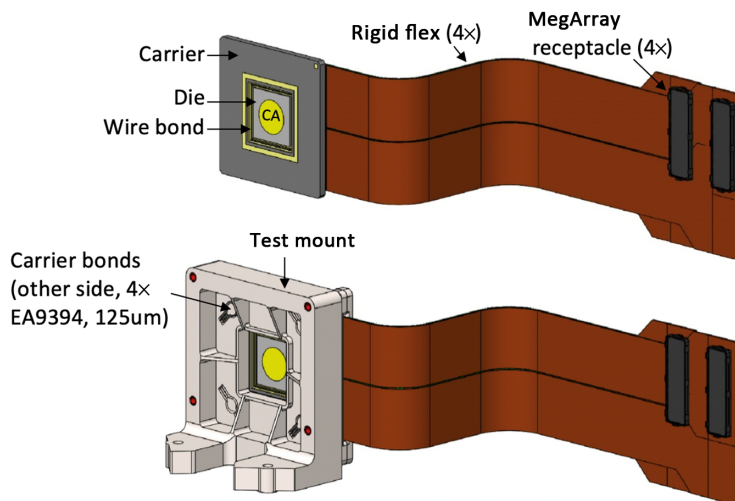
Fig. 3 Front schematic of the ceramic chip carrier, mount, and rigid flex cables designed for the 2K MEMS DMs.
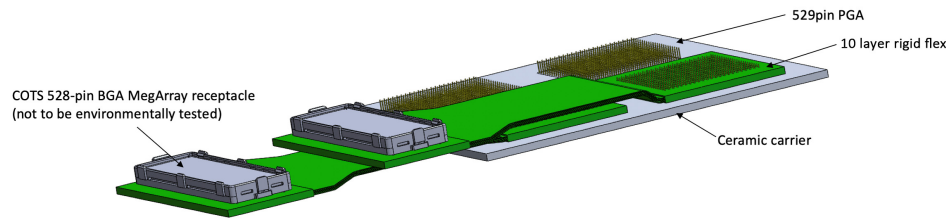
Fig. 4 PGA assembly at the back of the ceramic chip. The MEG-Array connector was not considered part of the random vibe test.

3 Procedure

3.1 Testing Overview

Both DUT 1 and 2 underwent a battery of tests before and after exposure to random vibrations. The carrier, die, die bonds, PGA joints, and carrier to test mount bonds were inspected in all phases. The actuator functionality and performance were tested using the steps outlined below. The MEG-Array connectors and receptacles are not envisioned as part of the flight system and are therefore not included in our analysis. The workflow of these experiments for both DUTs is illustrated in Fig. 5. Results of these tests are described in Sec. 4.

3.2 Infrared Inspection

Before applying the face sheet coating to DUT 1, both DUTs were inspected at BMC using transmissive infrared microscopy. The system was automated to translate the DM and image many actuators in sequence. To achieve this, a MLS203 fast $X - Y$ stage was installed on a BX51 Olympus microscope. The microscope was also equipped with a MFC1 Motorized Microscope focus controller to focus either on the wiring or on the mirror layer. The wiring layer was inspected on the entire die of dimension 32.8×32.8 mm by steps of 400 μm (size of the actuator pitch) for a total of 6224 images. The mirror layer inspection was restricted to the device area to image each actuator individually, and 4080 images were taken in a serpentine clockwise path. In total, 10,804 images were recorded per DM to be compared before and after the random vibe in case of failure. DUT 2 had three actuators with clearly visible defects just after fabrication (see the infrared image of an anomalous actuator in Fig. 14).

3.3 Functional Testing

DUT 1 was then coated, and both DMs were sent to the HCIT facility at JPL for testing. Functional testing was done using a Fizeau interferometer (Zygo Verifire). The DMs were placed inside a plastic enclosure that was purged with a continuous flow of dry air to maintain a relative humidity of <30% during operation and to avoid any electrostatic discharge event.[17] The devices were connected through the MEG-Array connectors to a commercial 14-bit electronics provided
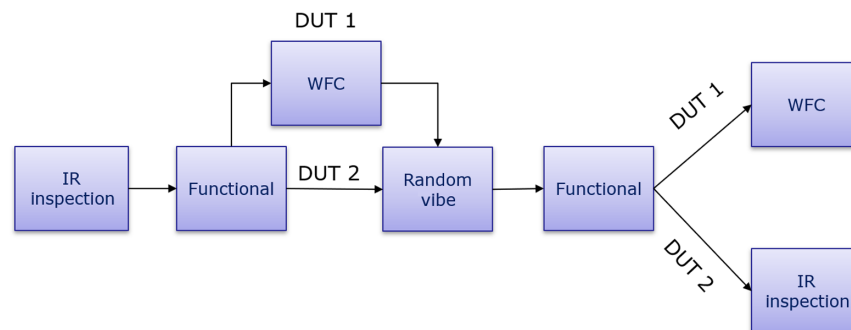
Fig. 5 Testing workflow. The tests before exposure to random vibrations consisted of an IR microscope inspection and functional tests using a Fizeau interferometer. DUT 1 was also used for WFC performance testing on a coronagraph testbed. After the random vibe, each DM was functionally testing using an interferometer. DUT 1 was then used for WFC performance testing, and DUT 2 was inspected using the IR microscope.

by BMC for the 2K-DM to perform a battery of functional spatiotemporal tests. The input voltage was limited to 90 V.

The HCIT team developed a series of functionality tests aimed at highlighting defective actuators before and after the random vibe that were sorted in several categories. A "pinned" actuator is fixed to its unpowered position and is easily noticeable when uniform voltage is applied to the DM. A "free-floating" actuator does not move through electric commands but remains free to move to follow the displacements of its neighbors. "Tied" actuators occur when more than one actuator responds to a command sent to a single actuator index. A "weak" actuator moves significantly less than its neighbors with the same command. Finally, an "anomalous" actuator can be any of the above categories or otherwise defective. The standard functionality test process consists of the routines described below. For each surface measurement recorded by the Zygo interferometer, the uncommanded surface was subtracted, and piston, tip, and tilt aberrations were removed from the data in post-processing.

The functionality test routines are as follows.

3.3.1 *Applying a uniform voltage*

A uniform voltage is applied to all actuators. The measurement is taken at increasing voltage levels. Pinned actuators are particularly apparent in the resulting data.

3.3.2 *Poking individual rows and columns*

A uniform voltage is applied to the actuators in the same rows and then columns (100 measurements for a 2K MEMS DM). This highlights anomalous actuators and helps determine their index. This is also used to confirm the mapping between high-voltage channels in the electronics and the actuators. Tied actuators are also noticeable in the data, except if they are located in the same row or column.

3.3.3 *Poking grids of actuators*

The actuators are divided in 4×4 regions and one actuator from each region is poked simultaneously such that it creates a regular grid, with a large enough separation to avoid coupling effects. This process is repeated 16 times to cover all of the DM actuators. Free-floating actuators are particularly visible in the resulting data. This is a standard calibration routine for our DMs because it can be used to estimate the voltage to surface displacement conversion for each actuator using a limited number of images.

3.3.4 *Poking individual actuators*

The actuators are poked one-by-one. This is used to find the index of each anomalous actuator that was noticed in earlier stages and to solve ambiguities.

3.3.5 *Stability measurement*

First, a uniform voltage is applied once to all actuators, and one measurement is recorded every minute for 2 h (uncommanded stability). Second, a uniform voltage is applied every minute for 2 h immediately followed by a measurement with the interferometer (commanded stability). These tests aim to measure DM drifts over time. The low-order spatial aberrations are filtered to monitor the drift of individual actuators. The mean of the recorded time series is subtracted for each image, and the standard deviation is measured. An animation of the processed images is also visually inspected for anomalies.

3.3.6 *Repeatability measurement*

The voltage is cycled between zero and a uniform voltage for all actuators every 5 s for 50 s, and a measurement is recorded after each cycle. This aims to highlight any hysteresis due

to the DM or the electronics. The images are processed the same way as the stability measurements.

3.3.7 *Temporal response measurement*

We apply zero volts to the DM followed by a uniform bias. Ten measurements are then recorded as quickly as possible with the interferometer for about 20 s. The aim is to identify slow responding actuators. One measurement takes about 2 s on average, which prevents the detection of temporal frequencies higher than 0.25 Hz. The low-order spatial aberrations are removed in post-processing and the time series is subtracted by its last image to highlight any differences in our visual inspection.

3.3.8 *Calibrating the DM*

The grid of actuators is used to determine the locations of each actuator with respect to the Zygo beam and the surface displacement for a given voltage. The DM is then flattened iteratively using the information collected in this way. The linear or quadratic voltage-to-surface height conversion is then measured at the flat DM state, which is then used in the model for the wavefront sensing and control (WS&C) method used to create the DH in the coronagraph instrument.

3.4 Performance Testing

DUT 1 was also tested for high-contrast imaging purposes using the In-Air Coronagraph Testbed (IACT)[18] in the HCIT facility at JPL. The IACT optical layout is shown in Fig. 6. A 637 nm monochromatic light source was injected into the enclosed testbed through a single mode fiber to simulate a star. A charge six-Vector Vortex Coronagraph (VVC) was used to limit the sensitivity to low-order wavefront aberrations due to air turbulence.[19–22]

The injected light was passed through a linear polarizer (LP) and a quarter wave plate (QWP) to circularly polarize the light source upstream of the focal plane mask (FPM). The LP had an extinction ratio of 10^5, and the QWP had a retardance of 0.24λ at 637 nm. The off-axis parabola (OAP) 1 then collimated the beam and reflected it toward a 18.48 mm pupil, immediately followed by DUT 1. There were 46.2 actuators across the beam at the DM. Similar to the functional test described above, DUT 1 was placed inside a plastic box with a continuous flow of dry air to reduce the humidity. To limit air turbulence, the flow was optimized to reach a relative humidity of 25% to meet the DM specification. A Fluke DewK thermo-hygrometer was inserted in the dry box to actively sense the humidity level through a software watchdog. The box had an opening on the front side to allow the beam to reflect off the DM to the 1524 mm focal length OAP2 that
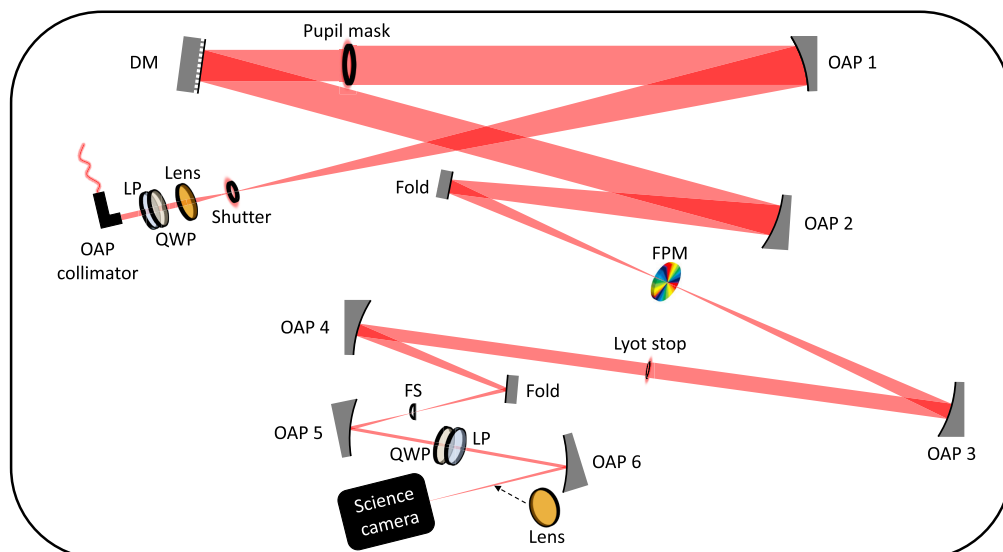
Fig. 6 Schematic of the optical layout of IACT in the HCIT facility at JPL. Not to scale.

focused the light on the VVC FPM. The FPM was fixed to a three-axis mount. The diffracted light was then reflected on the 762 mm focal plane OAP3 and blocked by a Lyot Stop (LS) of diameter 7.5 mm on a two-axis mount. Considering the magnification of the OAPs, the LS diameter was 81.2% of the pupil image.

A "D" shaped field stop (FS) of size 3 to $10\lambda/D$ was added in the downstream conjugated focal plane. The purpose of the FS was to enhance the contrast in the final focal plane at the camera by minimizing stray light or photoelectrons inside the corrected regions adjacent to saturated regions. The FS was placed on a three-axis mount to optimize focus and can be moved in and out for calibration purposes. The dark images that are later subtracted from the DH images were recorded by fully blocking the light at the FS plane.

After the FS, the beam was then collimated by OAP5 to pass through another set of QWP and LP that minimizes the incoherent leakage caused by the imperfect retardance in the VVC FPM. The rotation angles of the QWP + LP were optimized by minimizing the signal on the science detector with the VVC FPM fully removed from the beam. Finally, the OAP6 directed the light to the science detector where the final image was formed. A neutral density filter wheel can be used for calibration purposes, for instance, to prevent the over-exposure of the unocculted PSF used for calibration, and it has an optical lens to allow for pupil imaging. The science camera Andor Neo sCMOS electrically cooled to −40°C, and the generated heat was removed with a water cooler. The camera was mounted on a single-axis stage to control the focus. The pixel pitch was 6.5 μm, and the resolution of the focal plane images was 24.7 pixels per λ/D.

Standard WS&C algorithms and calibration procedures dedicated to high-contrast imaging were used to minimize the simulated stellar intensity at the detector plane and improve the raw contrast level (intensity of the attenuated starlight normalized by the maximum of the unocculted PSF).[23] Phase retrieval algorithms based on both Gerchberg–Saxton formalism[24] and the fitting of low-order Zernike modes were used to flatten the DM and calibrate its response. At least three images close to the focal plane and three images close to the pupil plane were used to run the algorithm. After flattening the DM, the Strehl ratio of the unocculted PSF was very close to 1.0. The VVC FPM and the LS were automatically centered on the beam iteratively through the acquisition of pupil images. Dark images and off-axis PSFs were then recorded, and the FS was introduced in the beam to allow the desired off-axis DH region to pass through.

Wavefront sensing and WFC were performed, respectively, with pair-wise probing (PWP) and electric field conjugation (EFC)[25,26] through FALCO software.[27] Both algorithms require a high-performance DM to achieve contrast levels of ~10^{-8}. The DH region where the stellar residuals are attenuated is defined by the FS aperture that goes from 3 to $10\lambda/D$. Although the contrast improves in the DH, the exposure time on the science camera is increased from 100 to 300 s to maintain a sufficient signal-to-noise ratio. The β-bumping technique[28] is regularly used to achieve the best possible coherent contrast in the DH region. The raw contrast in the DH is intricately linked to the DM performance. Performance testing results for DUT1 are presented in Sec. 4.1.

3.5 Random Vibration Environment

In the previous work, we demonstrated the robustness of actuators that were surrounded by functional actuators under flight-like thermal cycles and vibrations as well as the compatibility of partially functional 50×50 MEMS DMs with vacuum environments.[16] This work expands the previous study in that we specifically test the robustness of actuators at the vicinity of defective actuators as well as the fully functional 50×50 MEMS DMs. The DMs and their respective mounts were shaken at JPL on a 10-in. cube shaker. The flex cable was fixed to the edge of the mount with a flex clamp, whereas the other end of the flex was curled loosely and taped down onto the moving platform of the shaker to avoid any damage. Particle contamination and humidity were controlled during the test to ensure that the DMs were not subject to alternative sources of electric degradation and failure,[29] as suspected in previous studies.[15] The applied signal ranged between 20 and 2000 Hz, which corresponds to typical frequency ranges for most launch vehicles. The temporal acceleration spectral density of the vibrations in each of the three spatial axes was between 0.01 and 0.4 g^2/Hz and is shown in Fig. 7. The DMs therefore underwent 11.7 gRMS over all frequencies for 2 min per axis. This qualification test is conservative to
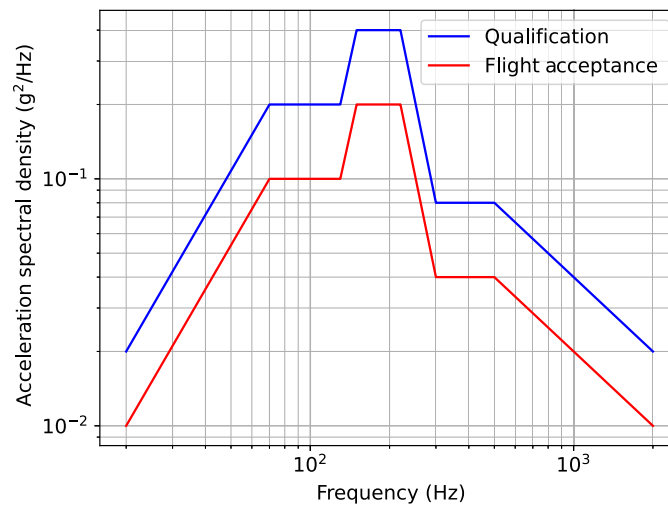
**Fig. 7** Power spectral density of the vibration experienced by the MEMS DMs in the three axes.

any potential launch vehicles and surpasses the flight acceptance followed by the RST Coronagraph Instrument specifications.

4 Test Results

4.1 DUT 1

DUT1 is a 100% yield device intended to validate that a fully functioning MEMS DM passes random vibration testing. The criteria of success are visual inspection of the structure; the actuator responsiveness, stroke, and voltage-to-displacement gain; and the ability to create a DH at relevant contrast levels ($\sim10^{-8}$). This section compares the results of functional and performance testing before and after the random vibration at JPL.

Figure 8 represents one of the 16 regular grids of actuators that were poked during the functional test of DUT1 before and after the random vibe test. The image resolution has been slightly decreased after the vibe because we did not ensure same Zygo zoom settings before and after the random vibe test. Such a resolution remains acceptable for direct comparison with pre-vibe data because we have many more than the required 4 pixels per DM actuator. As in the 15 other grids, the behavior of the actuators was identical before and after the random vibe regardless the applied
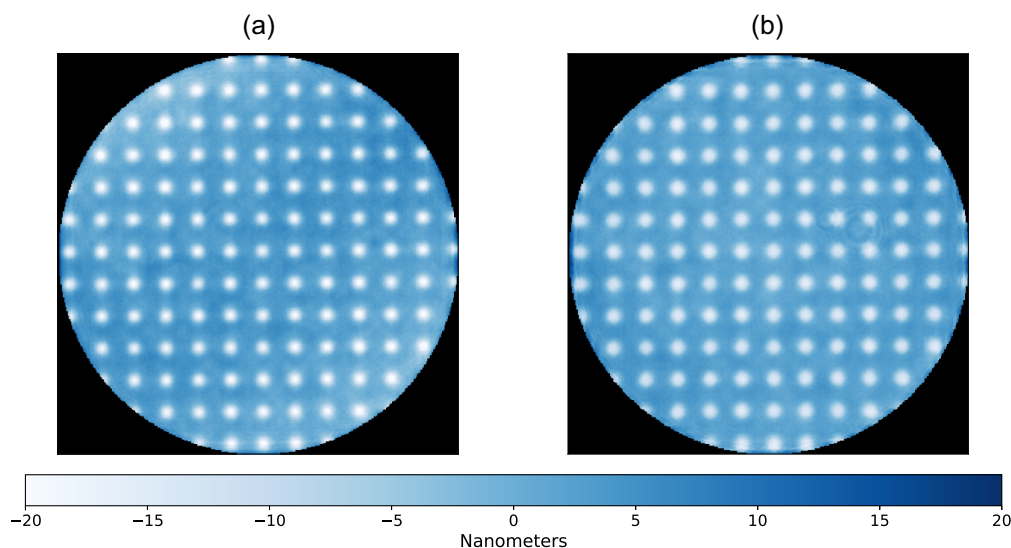
Fig. 8 Optical path difference (in nanometers) that corresponds to a functional test in which a regular grid of actuator was poked (a) before and (b) after the shaking of DUT1.

voltage. No anomaly in the influence function shape nor displacement of the DM surface occurred. After DM flattening, the final shape was measured to be 3.41 nm RMS wavefront error before and 3.37 nm RMS after the random vibe. Around the flat setting, the quadratic relationship between the surface displacement amplitude of each actuator and the applied voltage remains identical before and after the vibe. None of the functional tests performed showed any anomalies on DUT1 either before and after the DM was random vibed.

After functional testing, DUT1 was installed on IACT to test the DM performance in a coronagraph instrument. Figure 9 shows the normalized intensities in the science image before and after the random vibe and after a few dozen WS&C iterations. The mean contrast in the DH is 1.19×10^{-8} (before the random vibe) and 9.53×10^{-9} (after the random vibe), and the spatial standard deviation is equal to 1.42×10^{-8} and 1.28×10^{-8}, respectively. The mean coherent contrast is equal to 3.80×10^{-9} before and 4.34×10^{-9} after with a respective standard deviation of 3.71×10^{-9} and 3.86×10^{-9}. The small difference in coherent contrast is explained by a slightly higher internal turbulence on the testbed after the random vibe. We also observe in Fig. 9 some horizontal artifacts that result from diffraction effects caused by a slight misalignment of the FS in the z direction. These highly localized effects did not impact convergence of the PW + EFC algorithm nor the computation of contrast performance. The decrease of flux after the random vibe might induce an underestimation of the mean incoherent intensity leading to a slight overestimation of the contrast performance after the random vibe.

Figure 10 overlays the radial profile of each total intensity image, the mean contrast of which is calculated in annulus of $\lambda/8D$. On the one hand, both Figs. 9 and 10 emphasize that IACT performance are limited at low separations by an Airy pattern. This pattern is not sensed by PWP. This pattern is known to be an incoherent leakage due to manufacturing defects in the VVC FPM and in the LP and QWP.[23] This leakage could be further reduced by improving the retardance error in the QWP and the extinction of the LP that are currently used. On the other hand, the coherent component in the DH was measured below 10^{-8} in both cases, and its speckle intensity structure was modified at each iteration. We therefore attribute the remaining coherent component to the internal turbulence in IACT on timescales of a single WS&C iteration. This effect could be reduced on IACT by lowering the dry air-flow or by installing an additional WS&C system to specifically control low-order spatial aberrations at higher temporal frequencies.[30] Nonetheless, from the results of both the performance and functional test on DUT1, we can conclude that DUT1, a 100% functional 2K MEMS DM, survived random vibrations similar to a launch vehicle.

4.2 DUT 2

DUT2 had a few defective actuators and no metallic coating with the intention of testing the hypothesis that anomalous actuators can propagate to neighbors during rocket launch. DUT2 is not coated to allow for IR inspection after the random vibe. DUT2 also underwent the battery of functional tests described above, but it was not used for performance testing.
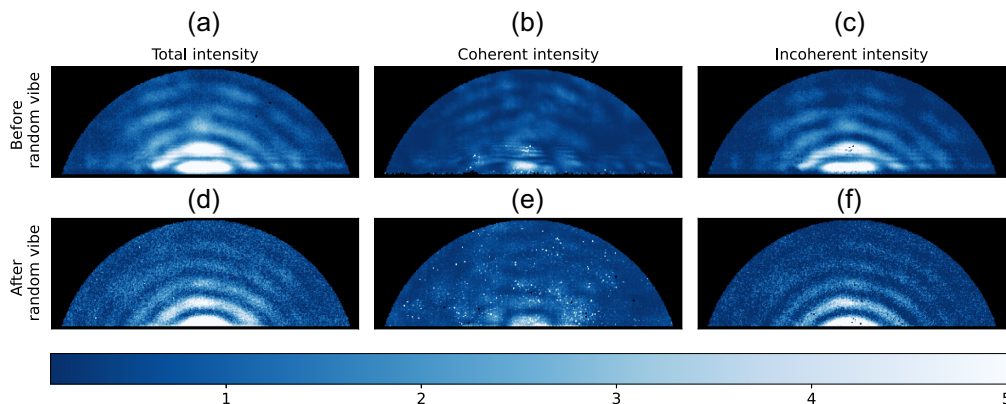

Fig. 9 Post-WS&C contrast maps ($\times 10^8$) (a)–(c) before and (d)–(f) after the DUT1 underwent flight-like shaking. (a), (d) total; (b), (e) coherent; and (c), (f) incoherent intensities are presented. The exposure time for both total intensity images is 300 s, but the source injection unit has been moved between the experiments, explaining the noise discrepancy.
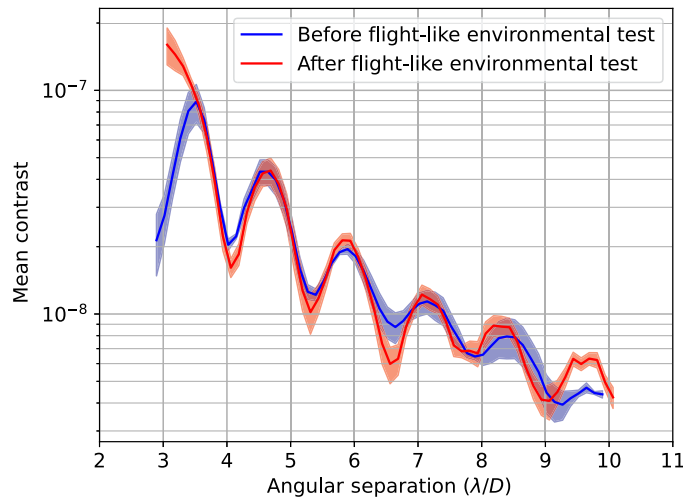
Fig. 10 Post-WS&C radial profiles of the raw contrast on the science detector before (blue) and after (red) the DUT1 underwent random vibe testing.

In pre-vibe function testing, DUT2 was found to be ∼99.3% functional (see in Fig. 11). It had three pinned actuators, two couples of tied actuators, and two couples and one triplet of weak and tied actuators (the voltage to amplitude gain of which is divided by the number of associated actuators). One result of the functional test is shown in Fig. 12, in which the same grid of actuators was poked with respect to the grid in Fig. 8. The poke grid measurements show that DUT2 did not change behavior at the actuator level. As an example, Fig. 13 shows the deflection for neighbors of one defective actuator (index 1283) while applying individual voltage of 0.025 BMC unit on top of a flat bias of 0.05 BMC unit. Their influence functions were fitted with a Gaussian with the maximum amplitude being reported in this plot. Error bars are computed as the standard deviation of the measured amplitude for the eight neighbors. The deflection of 1283 actuator's neighbors remains identical before and after random vibration: failure did not
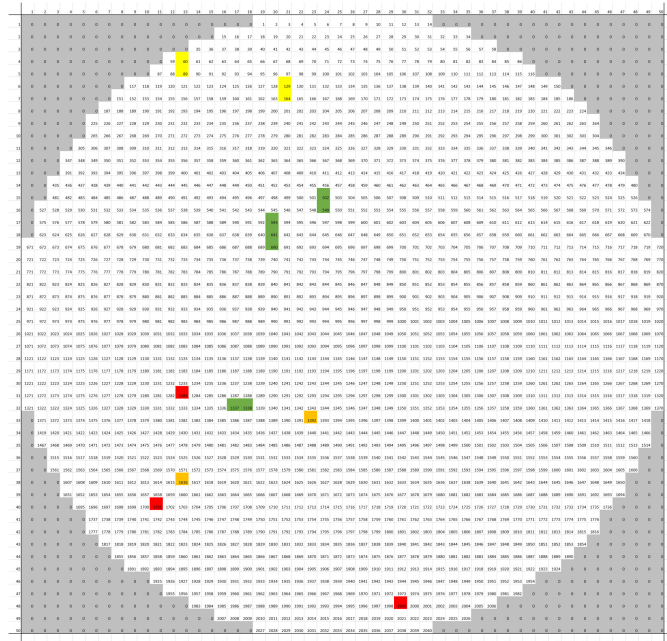
Fig. 11 Grid of DUT2 actuators. Yellow: tied actuators (60–89, 129–164). Green: tied and weak actuators (502–549, 593–641–690, 1337–1338). Red: pre-vibe pinned actuators (1283, 1701, 1999). Orange: post-vibe pinned actuators due to poor connections at the MEG-Array connectors level (1392, 1616).

(a)   (b)
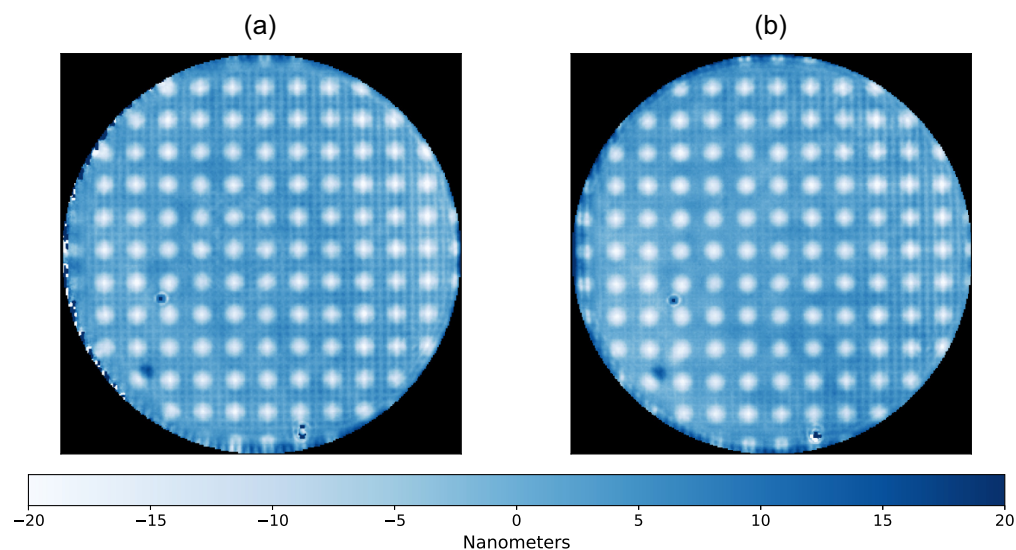
Fig. 12 Optical path difference (in nanometers) that corresponds to a stage of functional test, in which a regular grid of actuator was poked, before (left) and after (right) random vibe testing of DUT2.
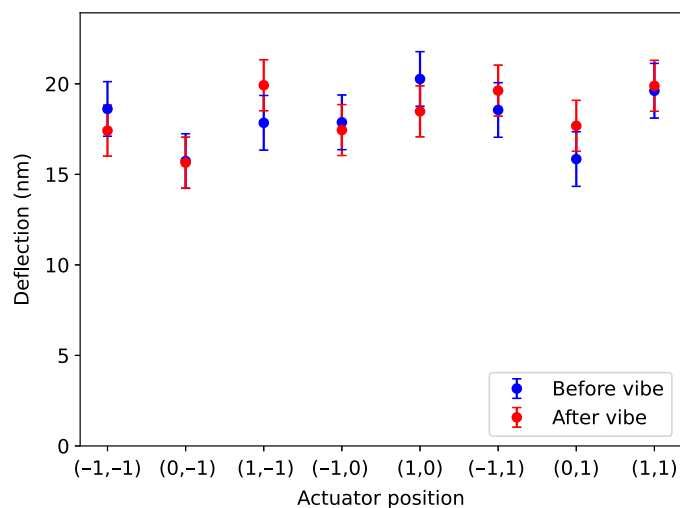

Fig. 13 Deflection of actuator 1283s neighbors. We applied 0.025 BMC unit on these individual actuators on top of 0.05 BMC unit applied to all DUT 2 actuators.

propagate during rocket launch simulation. These results were confirmed by the remaining functional tests, described in Sec. 3.3.

Preliminary tests with post-vibe DUT2 presented new anomalous actuators with respect to pre-vibe, particularly tied characteristics. After further investigation, we realized that these anomalies were due to poor connections at the MEG-Array connectors level rather than the DM. Indeed, the connectors were disconnected before the random vibe and then reconnected for the functional tests. This process is sensitive because the pins can be easily bent if the connectors are not carefully handled. The defective connectors were fixed either by disconnecting and then reconnecting the faulty MEG-Array connector or by replacing the connector savers if the initial reconnection appeared unsuccessful. The state of the MEG-Array connectors was carefully inspected throughout the whole process. Given the challenges faced by our team related to connectors, we advocate for the development of more robust high-density connector technology and more practical DM driver electronics.[8]

We also imaged the initial defective actuators and their neighbors with the infrared microscope to confirm that the DM was not affected by the simulated rocket launch. No changes to the
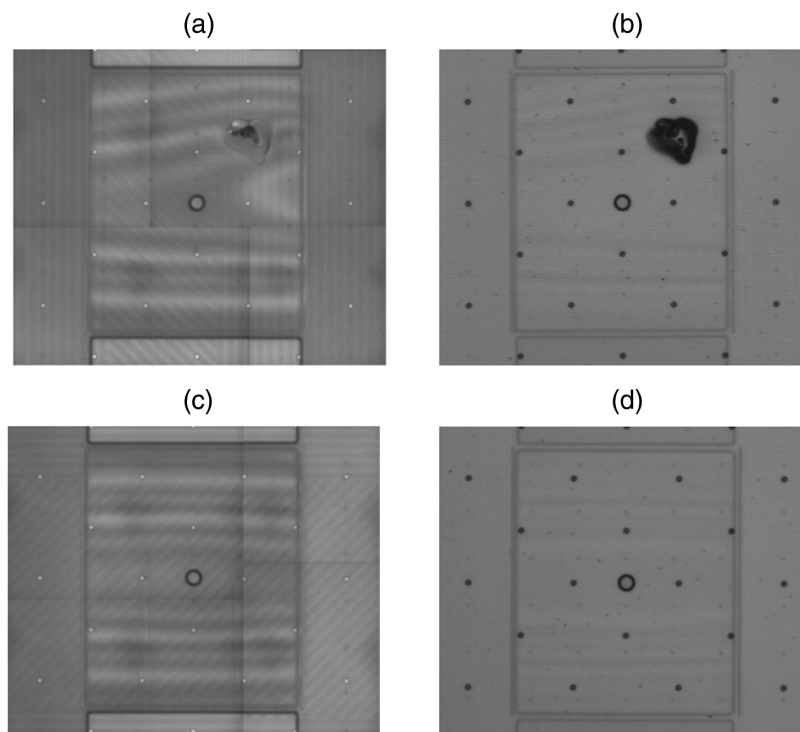
Fig. 14 (a), (c) Pre-vibe and (b), (d) post-vibe infrared images of both (a), (c) a pinned actuator and (b), (d) the direct neighbor of a pinned actuator. (a) and (c) are focused on the wiring layer. (b) and (d) are focused on the mirror layer in reflection due to the DM package.

anomalous actuators nor their neighbors were notice during the post-vibe infrared inspection. Figure 14 shows the infrared image of one tied actuator as well as the neighbor of another, focusing either on the wiring layer or on the mirror layer, before and after the random vibe. The anomaly shown on the pinned actuator is apparent on both layers. The comparison of the images before and after the random vibe shows that the damage has not propagated from the initial defect. The second set of images shows that none of the neighbor carrier, die, die bonds, PGA joints, nor actuators were affected by the random vibe test. From these results, we saw no evidence that anomalous actuators propagate to neighbors during the random vibe.

5 Conclusion

As part of a NASA SBIR, BMC and JPL jointly developed a new fabrication process for 50×50 MEMS DMs. Two of these DMs underwent a battery of experiments to test their ability to survive in a launch vehicle. We have demonstrated that (1) a 100% functional 2K MEMS DM maintains 100% functionality and (2) anomalous actuators do not propagate to neighboring actuators after undergoing launch-level vibrations. BMCs 2K continuous face sheet MEMS DMs passed three-axes random vibe environmental testing at bounding launch loads encompassing those of future launch vehicles. Acoustics, shock, and radiation testing remain key steps toward achieving TRL 6 for BMC's MEMS DM technology. In addition, we recommend further development of connector systems for flight DMs to lower the risk of creating anomalous actuators during future DM testing, flight qualification, and mission development.

space-based applications," Proc. SPIE 11823, Techniques and Instrumentation for Detection of Exoplanets X, 118230M (1 September 2021); doi: 10.1117/12.2594263.

References

1. National Academies of Sciences, Engineering, and Medicine, *Pathways to Discovery in Astronomy and Astrophysics for the 2020s*, The National Academies Press, Washington, DC (2021).
2. F. Malbet, J. W. Yu, and M. Shao, "High-dynamic-range imaging using a deformable mirror for space coronography," *Pub. Astron. Soc. Pacific* **107**, 386 (1995).
3. J. T. Trauger et al., "Coronagraph contrast demonstrations with the high-contrast imaging testbed," *Proc. SPIE* **5487**, 1330–1336 (2004).
4. M. A. Ealey and J. T. Trauger, "High-density deformable mirrors to enable coronographic planet detection," *Proc. SPIE* **5166**, 172–179 (2004).
5. A. Wirth et al., "Deformable mirror technologies at AOA Xinetics," *Proc. SPIE* **8780**, 87800M (2013).
6. T. Bifano, "Adaptive imaging: MEMS deformable mirrors," *Nat. Photonics* **5**, 21–23 (2011).
7. R. Morgan et al., "MEMS deformable mirrors for space-based high-contrast imaging," *Micromachines* **10**(6), 366 (2019).
8. E. Bendek et al., "Microelectromechanical deformable mirror development for high-contrast imaging, part 1: miniaturized, flight-capable control electronics," *J. Astron. Telesc. Instrum. Syst.* **6**, 045001 (2020).
9. N. J. Kasdin et al., "The Nancy Grace Roman Space Telescope Coronagraph Instrument (CGI) technology demonstration," *Proc. SPIE* **11443**, 114431U (2020).
10. P. Baudoz et al., "Optimization and performance of multi-deformable mirror correction on the THD2 bench," *Proc. SPIE* **10706**, 107062O (2018).
11. C. Mejia Prada, E. Serabyn, and F. Shi, "High-contrast imaging stability using MEMS deformable mirror," *Proc. SPIE* **11117**, 1111709 (2019).
12. A. J. E. Riggs et al., "High contrast imaging with MEMS deformable mirrors in the Decadal Survey Testbed," *Proc. SPIE* **11823**, 118230S (2021).
13. B. S. Gaudi et al., "The Habitable Exoplanet Observatory (HabEx) mission concept study final report," https://www.jpl.nasa.gov/habex/pdf/HabEx-Final-Report-Public-Release.pdf (2019).
14. The LUVOIR Team, "The large UV Optical Infrared Surveyor (LUVOIR) final report," https://asd.gsfc.nasa.gov/luvoir/resources/docs/LUVOIR_FinalReport_2019-08-26.pdf (2019).
15. P. Bierden, *MEMS Deformable Mirror Technology Development for Space-based Exoplanet Detection*, SAT Milestone Rep. (2022).
16. C. Mejia Prada et al., "Environmental testing of high-actuator-count MEMS deformable mirrors for space-based applications," *Proc. SPIE* **11823**, 118230M (2021).
17. K. M. Morzinski et al., "MEMS practice: from the lab to the telescope," *Proc. SPIE* **8253**, 825304 (2012).
18. W. Baxter et al., "Design and commissioning of an in-air coronagraph testbed in the HCIT facility at NASA's Jet Propulsion Laboratory," *Proc. SPIE* **11823**, 118231S (2021).
19. G. Foo et al., "Optical vortex coronagraph," *Opt. Lett.* **30**(24), 3308–3310 (2005).
20. D. Mawet et al., "Optical vectorial vortex coronagraphs using liquid crystal polymers: theory, manufacturing and laboratory demonstration," *Opt. Express* **17**(3), 1902–1918 (2009).
21. D. Mawet et al., "The Vector Vortex Coronagraph: sensitivity to central obscuration, low-order aberrations, chromaticism, and polarization," *Proc. SPIE* **7739**, 773914 (2010).
22. G. Ruane et al., "Vortex coronagraphs for the Habitable Exoplanet Imaging Mission concept: theoretical performance and telescope requirements," *J. Astron. Telesc. Instrum. Syst.* **4**(1), 015004 (2018).
23. G. Ruane et al., "Broadband Vector Vortex Coronagraph testing at NASA's high contrast imaging testbed facility," *Proc. SPIE* **12180**, 1218024 (2022).
24. R. A. Gonsalves, "Phase retrieval and diversity in adaptive optics," *Opt. Eng.* **21**(5), 829–832 (1982).
25. P. J. Bordé and W. A. Traub, "High-contrast imaging from space: speckle nulling in a low-aberration regime," *Astrophys. J.* **638**, 488–498 (2006).
26. A. Give'On et al., "Broadband wavefront correction algorithm for high-contrast imaging systems," *Proc. SPIE* **6691**, 66910A (2007).
27. A. Riggs et al., "Fast linearized coronagraph optimizer (FALCO) I: a software toolbox for rapid coronagraphic design and wavefront correction," *Proc. SPIE* **10698**, 106982V (2018).
28. E. Sidick et al., "Sensitivity of WFIRST coronagraph broadband contrast performance to DM actuator errors," *Proc. SPIE* **10400**, 1040006 (2017).
29. Y. Huang et al., "MEMS reliability review," *IEEE Trans. Device Mater. Reliab.* **12**, 482–493 (2012).
30. F. Shi et al., "Low-order wavefront sensing and control for WFIRST-AFTA coronagraph," *J. Astron. Telesc. Instrum. Syst.* **2**, 011021 (2016).

Biographies of the authors are not available.